

Physics-Informed Neural Network-Based Control for Grid-Forming Converter's Stability Under Overload Conditions

Abhay Kumar, Member, IEEE, Dushyant Sharma, Member, IEEE, and Mayukha Pal, Senior Member, IEEE

Abstract—Grid-forming converters (GFCs) are pivotal in maintaining frequency and voltage stability in modern distribution systems. However, a critical challenge arises when these converters encounter sudden power demands that exceed their rated capacity. Although GFCs are designed to manage DC source saturation and limit excessive AC currents, their ability to ensure sufficient power delivery under such constraints remains a significant concern. Existing studies often overlook this limitation, potentially compromising system stability during high-demand scenarios. This paper proposes a control strategy based on a physics-informed neural network (PINN) to improve GFC performance under overloaded conditions, effectively preventing switch failures and mitigating DC source saturation. The proposed approach outperforms conventional methods by maintaining stable voltage and frequency, even under significant load increases where traditional droop control alone proves inadequate. The post-disturbance operating point of GFCs remains unchanged using PINN-based control. Peak voltage deviation observed during transient reduced to 42.85%. Furthermore, the proposed method ensures that the rate of change of frequency (ROCOF) and the rate of change of voltage (ROCOV) remain within acceptable limits, significantly improving system resilience in inertia-less power networks.

Index Terms—Current Limitation, droop control, DC source saturation, grid-forming converter (GFC), physics-informed neural network (PINN), micro-grid (MG)

I. INTRODUCTION

A. Problem and Importance

RENEWABLE energy sources, such as photovoltaics (PV) and batteries, integrated via grid-following inverters, face challenges like low inertia and dependence on the grid, limiting their functionality in islanded systems. Grid-forming converters, functioning as voltage sources with fixed frequency, offer a solution by enabling island operation and maintaining power balance. Advanced control strategies are essential for effectively integrating into modern power systems [1]. Comparative studies show grid-forming converters surpass grid-following counterparts in autonomy and frequency stability [1]. Grid-forming control strategies have been extensively studied to enhance the stability and performance

of inverter-based power systems. As discussed in [2], droop control is a widely adopted method for managing parallel-connected inverters in standalone AC supply systems. State-space modeling techniques for autonomous microgrid inverters are explored in [3], along with a sensitivity analysis that aids in system assessment. Synchronverters, introduced in [4], emulate synchronous generators and offer improvements in harmonic distortion and the fluctuating amplitude of grid-side currents, as presented in [5]. Equivalences between virtual synchronous machines (VSM) and frequency droop control are examined in [6], while virtual oscillator control (VOC), introduced in [7], stabilizes interconnected inverters by mimicking nonlinear oscillator dynamics. A comparative study in [8] highlights VOC's superior stability performance in the time domain over droop control for interconnected inverters. Transmission line effects analyzed in [9] reveal destabilizing impacts on multi-inverter systems, emphasizing the importance of properly tuning inverter control gains. Synchronous machine-inspired matching control is proposed in [10], while [11] explores various GFC strategies, including droop control, VSM, matching control, and dispatchable VOC (dVOC). Among these, matching control demonstrates improved frequency stability but shows a higher rate of change of frequency (ROCOF) under sudden large load conditions. All the methods discussed above provide stability to the system at nominal and rated power levels of the GFC. However, the stability of GFC under conditions involving DC source saturation and AC current limits has not been extensively explored, particularly in scenarios with sudden large power demands that exceed the GFC's rated power. To address this issue, [11] introduces a current limitation strategy that successfully stabilizes droop-controlled GFCs; however, this method affects the post-disturbance operating point of GFCs due to its threshold value being set below the rated value. Moreover, all these model-based controllers rely heavily on precise tuning and are optimized for predefined environments, limiting their adaptability to dynamic grid conditions.

B. Related Publication

The resilience of GFCs in inertia-less systems, particularly with appropriate DC-side and AC-side voltage and current regulation under diverse operating conditions, remains a key focus of this paper. Fully renewable power systems, increasingly reliant on inverter-based resources, face significant stability challenges, as highlighted in [12]. Enhancements to droop control, such as integral sliding mode control, address issues like

(Corresponding author: Mayukha Pal)

Mr. Abhay Kumar is a Data Science Research Intern at ABB Ability Innovation Center, Hyderabad 500084, India, and also a Ph.D. Research Scholar at the Department of Electrical Engineering, Indian Institute of Technology (ISM), Dhanbad 826004, IN.

Dr. Dushyant Sharma is an Asst. Professor with the Department of Electrical Engineering, Indian Institute of Technology (ISM), Dhanbad 826004, IN.

Dr. Mayukha Pal is with ABB Ability Innovation Center, Hyderabad 500084, IN, working as Global R&D Leader – Cloud & Analytics (e-mail: mayukha.pal@in.abb.com).

TABLE I
MODERN CONTROL TECHNIQUES USING GFM CONVERTERS: A COMPARISON BETWEEN 2020 AND 2024

Ref.	Proposed Control Approach	Controllable Device	Optimal Parameter Design	Control Features	Adaptability in inertia-less MGs	Transition Modes	DC Saturation	AC Current Limitation	Same post disturbance operating point
[11]	Decentralized frequency control scheme	Synchronous machine and multiple GFCs	[✓]	P/f droop	[X]	N/A	[✓]	[✓]	[X]
[17]	Decentralized adaptive frequency control scheme	Aggregate EV	[✓]	Adaptive P/f	[X]	N/A	N/A	N/A	N/A
[18]	Robust data-driven-based controllers	Distributed EVs	[✓]	Robust $P/f, P/V$	[X]	N/A	N/A	N/A	N/A
[19]	Adaptive PID-PSS	Aggregate synchronous generator	[✓]	Adaptive $P/f, P/V$	[X]	N/A	N/A	N/A	N/A
[20]	Unified model predictive fuzzy-based controller	Multiple voltage source converters	[✓]	Adaptive $P/f, Q/V$	[✓]	Seamlessly reconnect to MG	N/A	N/A	N/A
[22]	Robust-guided neural network	Distributed converter-interfaced resources	[✓]	Intelligent $P/f, Q/V$	[✓]	N/A	N/A	N/A	N/A
[23]	Neural network	Voltage source converter	[✓]	Intelligent $P/f, Q/V$	[X]	N/A	N/A	N/A	N/A
[24]	Physical-model-free intelligent framework	Renewable-based generations	[✓]	Intelligent optimal costs	[X]	N/A	N/A	N/A	N/A
[25]	Resiliency-guided intelligent-based GFM converter control	DSPEVs	[✓]	Adaptive intelligent $P/f, P/V, Q/V$	[✓]	Seamlessly reconnect to/disconnect from MG	N/A	N/A	N/A
This work	Physics-Informed Neural Network-Based Control for GFC	Renewable-based generations	[✓]	PINN with P/f droop	[✓]	Seamlessly reconnect to/disconnect from MG	[✓]	[✓]	[✓]

*Note that P/f : Active power for frequency control, P/V : Active power for voltage control, Q/V : Reactive power for voltage control. N/A: Not considered or reported, [✓]: Ensured, and [X]: Not ensured.

DC-side voltage collapse in GFCs, improving resilience under varying conditions [13]. Decoupling active and reactive power in GFCs using advanced techniques like multivariable control offers superior performance, as discussed in [14]. Model predictive control (MPC) integrated with VSM enhances system performance, reliability, and dynamic response, particularly in fluctuating grid environments, though further research is required to expand its application to other control strategies [15]. Additionally, adaptive inertia-based virtual synchronous generator designs for distributed generation (DG) inverters provide improved flexibility and performance in dynamic operating conditions [16].

PI controllers are commonly employed in GFC control loops to manage voltage and frequency variations [17]. However, precise tuning of PI controllers is challenging due to the complex mathematical modeling involved. To address this, data-driven control strategies have been introduced, simplifying the system modeling required for controller tuning. TABLE I highlights various studies on data-driven controllers using voltage source converters, identifying their features and limitations. For instance, Reference [18] reveals limitations in system adaptability in inertia-less microgrids. To enhance voltage and frequency stability in low-inertia microgrids, synchronous generator-integrated control loop signals have been explored [19]. Secondary and complementary control loops using fuzzy-based controllers have also been applied to

manage voltage and frequency in distributed converters [20] [21]. However, traditional controllers may struggle to maintain stability in weak microgrids under severe disturbances and uncertainties in distributed resources [22]. To address these challenges, advanced intelligent control techniques have been proposed. Robustness-informed deep learning neural networks [22] and convolutional neural networks (CNNs) [23] have shown promising results in improving microgrid voltage and frequency stability. Reference [24] examines the characteristics of renewable energy-powered microgrids and highlights the associated control challenges, with results indicating superior cost reduction compared to conventional methods. Additionally, a resilience-guided control framework proposed in [25] ensures seamless grid synchronization for stable voltage and frequency during unforeseen islanding conditions. Despite the progress achieved in data-driven control strategies, the studies summarized in TABLE I have not addressed DC source saturation and AC current limitations in GFCs that are necessary to protect semiconductor switches and the DC source under over-load conditions. This paper addresses this gap by investigating GFC stability under sudden overloading conditions, offering an improved control strategy that considers these critical factors.

C. Shortcomings and Significant Contributions

In conclusion, the data in Table I reveal significant gaps, including

- Previous research has not investigated the impact of current limitations in GFC during abrupt overload on the voltage and frequency stability of inertia-less microgrids using data-driven methods.
- Previous research has not investigated the impact of DC source saturation in GFC during abrupt overload on the voltage and frequency stability of inertia-less microgrids using data-driven methods.
- Applications of GFC with smooth grid connection and disconnection that take current limitation and DC source saturation into account have not been studied in previous studies using data-driven methods
- To properly manage voltage and frequency during islanding operations, GFC with current limiting and DC source saturation has not been investigated in previous studies.
- Previous research has not investigated the impact of current limitations and DC source saturation in GFC during abrupt overload on the voltage and frequency stability of inertia-less microgrids without influencing the post-disturbance operating point of the GFC.

To accomplish these goals, this study emphasizes the following contributions:

- A data-driven control approach based on a physics-informed neural network (PINN) is proposed for GFCs to enhance smooth transitions during islanding and grid-connected modes.
- The proposed PINN incorporates current limitation to protect the GFC during overload conditions without influencing the post-disturbance operating point of the GFCs.
- The proposed PINN ensures the stability of the microgrid by preventing saturation of the DC source during overload conditions.
- The proposed PINN maintains stability in inertia-less scenarios.

The remainder of this paper is organized as follows: Section II reviews the modeling of GFCs, including their control strategies. Section III presents the proposed Physics-Informed Neural Network (PINN) approach for enhancing GFC stability. The system under consideration, along with simulation-based analysis of various case studies, is discussed in Section IV. Finally, concluding remarks are provided in Section V.

II. MODELING OF GFC

We employ a test setup made up of power converters for our study.

A. Model of the converter

First, we look at the converter model in $\alpha\beta$ coordinates shown in Fig.1 [11].

$$C_d \dot{v}_d = i_d - G_d v_d - i_x \quad (1a)$$

$$L \dot{i}_{s,\alpha\beta} = v_{s,\alpha\beta} - R i_{s,\alpha\beta} - v_{\alpha\beta} \quad (1b)$$

$$C \dot{v}_{\alpha\beta} = i_{s,\alpha\beta} - i_{\alpha\beta} \quad (1c)$$

where, C_d is the DC link capacitance, G_d is the conductance that models DC losses, L is the filter's inductance, C is the

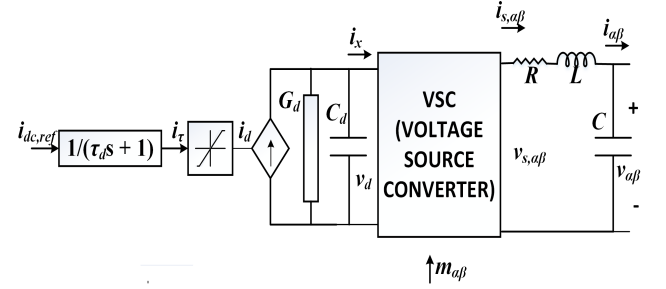


Fig. 1. Per phase equivalent model of the converter in $\alpha\beta$ coordinates

filter's capacitance, R is the filter's resistance, v_d is the DC voltage, i_d is the current flowing out of the controllable DC current source, $m_{\alpha\beta}$ is full bridge averaged switching stage model's modulation signal, $i_x = (1/2)m_{\alpha\beta}^T i_{s,\alpha\beta}$ (here $i_{s,\alpha\beta}$ is the node current of ac switching), $v_{s,\alpha\beta} = (1/2)m_{\alpha\beta}^T v_d$ (here $v_{s,\alpha\beta}$ is the node voltage of ac switching), $i_{\alpha\beta}$ is the output current and $v_{\alpha\beta}$ is the output voltage of the converter.

We use a first-order system to simulate the DC energy source's response time to create a realistic model

$$\tau_d \dot{i}_\tau = i_{dc,ref} - i_\tau \quad (2)$$

where, $i_{dc,ref}$ is the DC current reference, i_τ is the DC source-provided current and τ_d is DC source time constant. Additionally, the saturation function models the DC source current limitations

$$i_d = \begin{cases} i_\tau, & \text{if } |i_\tau| < i_{max}^d \\ \text{sgn}(i_\tau) i_{max}^d, & \text{if } |i_\tau| \geq i_{max}^d \end{cases} \quad (3)$$

where i_{max}^d is the maximum DC source current. It should be noted that for the DC source to facilitate bidirectional power flow, we implicitly assume the presence of some storage device. In actuality, the restriction imposed by (3) is equivalent to the current constraints of a PV/wind power generating system, a DC-DC converter, or an energy storage system. Notably, to safeguard its semiconductor switches, the converter must also restrict its AC current. The study uses an aggregate model consisting of 3 converter modules (i.e. number of converter, $n = 3$), each rated at 500 kVA, totaling 1.5 MVA. The resultant model will have output current as 3 times $i_{\alpha\beta}$ and output voltage as $v_{\alpha\beta}$ [11].

B. Control of GFC

Grid-forming control strategies regulate a converter using the reference current $i_{dc,ref}$ for the DC energy source and the modulation signal $m_{\alpha\beta}$ for the DC-AC conversion stage. The block diagram of the grid forming converter considered is shown in Fig. 2. The low-level cascaded control design is described as

1) *Control of DC Voltage:* The DC voltage control is managed by a current-controlled source, with a given DC current reference $i_{dc,ref}$ as

$$i_{dc,ref} = k_d(v_{d,ref} - v_d) + \frac{P_{ref}}{v_{d,ref}} + (G_d v_d + \frac{v_d \dot{i}_x - P}{v_{d,ref}}) \quad (4)$$

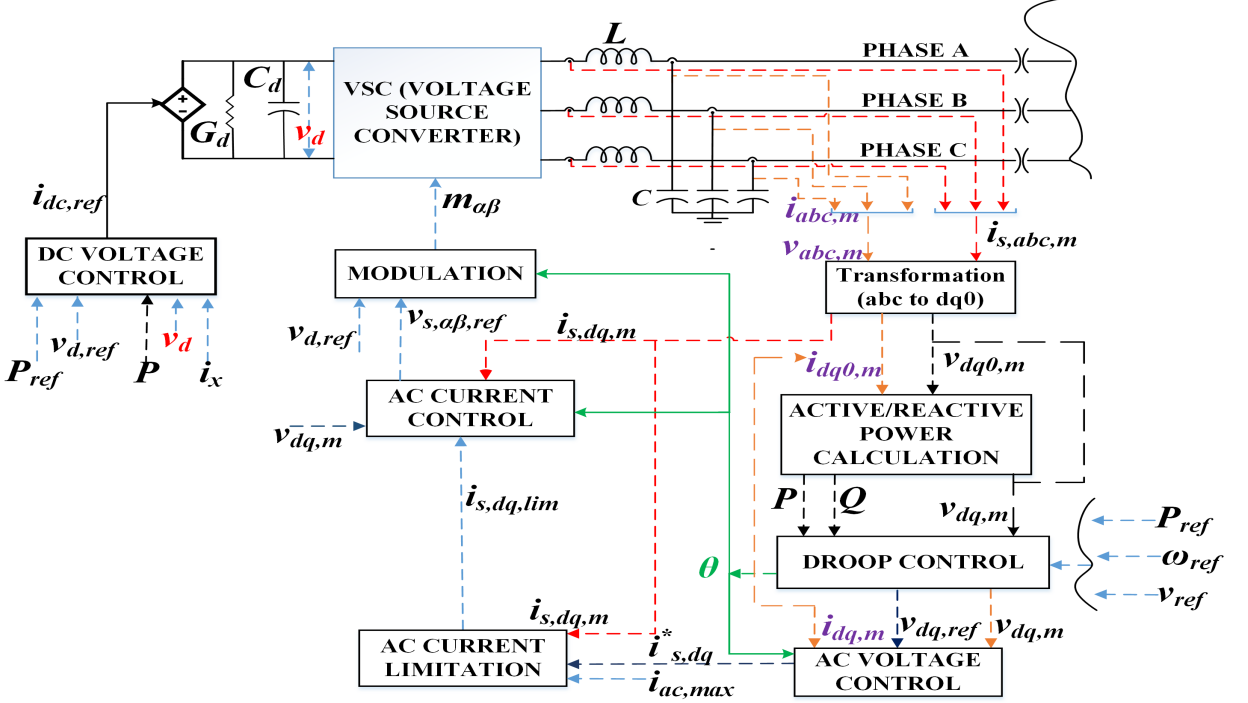


Fig. 2. Block Diagram of GFC Considered

where, k_d is DC voltage control gain, $v_{d,ref}$ is the reference DC voltage, P_{ref} is nominal active power injection, P is the active power injected into the grid and $v_d i_x$ is the DC power flowing into the switches. Therefore, to implement consistent DC voltage control, (4) is applied uniformly across all the control strategies discussed in this article.

2) *Control of AC Voltage:* As illustrated in Fig. 2, our converter control system employs a modulation signal $m_{\alpha\beta}$ (in some controls like matching control operating in $\alpha\beta$ co-ordinates is helpful [11]), which is determined by cascaded proportional-integral (PI) controllers. These controllers are implemented in dq-coordinates, rotating with the reference angle θ , and are designed to track the voltage reference $v_{dq,ref}$. The reference $i_{s,dq}^*$ for the switching node current $i_{s,dq,m}$ is calculated based on the voltage tracking error $v_{dq,ref} - v_{dq,m}$.

$$\dot{y}_{v,dq,m} = v_{dq,ref} - v_{dq,m} \quad (5)$$

$$i_{s,dq}^* = i_{dq,m} + C\omega T_2 v_{dq,m} + K_{v,p}(v_{dq,ref} - v_{dq,m}) + K_{v,i} y_{v,dq,m} \quad (6)$$

where, $y_{v,dq,m}$ is the integrator state, $v_{dq,ref}$ is the reference voltage in d-q reference frame, $v_{dq,m}$ is the output voltage in d-q reference frame, $i_{dq,m}$ is the output current in d-q reference frame, C is the filter's capacitance, ω is the measured frequency, $T_2 = \begin{bmatrix} 0 & -1 \\ 1 & 0 \end{bmatrix}$ (90° rotation matrix is denoted by T_2), $K_{v,p}$ is the diagonal matrix of proportional gain, $K_{v,i}$ is the diagonal matrix for integral gain.

3) *Limitation on AC Current:* As shown in Fig. 2, AC current limitation is essential to properly protect the switches

of the converter. Therefore, the reference current must remain below a specified current limit $i_{ac,max}$

$$i_{s,dq,lim} = \begin{cases} i_{s,dq}^*, & \text{if } \|i_{s,dq,m}\| \leq i_{ac,max} \\ w_i i_{s,dq}^*, & \text{if } \|i_{s,dq,m}\| > i_{ac,max} \end{cases} \quad (7)$$

where, $w_i = (i_{ac,max}/\|i_{s,dq}^*\|)$ and $i_{s,dq,lim}$ is the reference current with limitations. Limiting current is crucial for the stability margins and dynamics of grid-forming converter (GFC). In [29] and [30], it has been shown the importance of current limitation, and the maximum AC current is considered as 1.2 times the peak current (I_{peak}). This approach is implemented in the current study.

4) *Control of AC Current:* As shown in Fig. 2, the signal $i_{s,dq,lim}$ is tracked using a PI controller for the current $i_{s,dq,m}$

$$\dot{y}_{i,dq,m} = i_{s,dq,lim} - i_{s,dq,m} \quad (8)$$

$$v_{dq}^* = v_{dq,m} + Z i_{s,dq,m} + K_{i,p}(i_{s,dq}^* - i_{s,dq,m}) + K_{i,i} y_{i,dq,m} \quad (9)$$

where, $y_{i,dq,m}$ is the integrator state, v_{dq}^* is the reference voltage for switching, $K_{i,p}$ denotes the diagonal matrix of proportional gain, $K_{i,i}$ denotes the diagonal matrix of integral gain and $Z = L\omega T_2 + RI_2$ (here, I_2 is 2-D Identity Matrix, L is the filter's inductance and R is the filter's resistance). The modulation signal, $m_{\alpha\beta}$ is

$$m_{\alpha\beta} = \frac{2v_{s,\alpha\beta,ref}}{v_{d,ref}} \quad (10)$$

where $v_{s,\alpha\beta,ref}$ is $\alpha\beta$ co-ordinate image of reference voltage v_{dq}^* for switching.

5) *Droop Control:* Droop control mimics the speed droop characteristic of a synchronous machine governor, balancing power injection deviations with frequency variations

$$\dot{\theta} = \omega \quad (11)$$

$$\omega = \omega_{ref} + d_g(P_{ref} - P) \quad (12)$$

where d_g is the active power droop coefficient and ω_{ref} is the reference frequency. We use reactive power droop coefficient n_q , to control voltage as

$$v_{d,ac,ref} = v_{ref} - n_q Q \quad (13)$$

where, $v_{d,ac,ref}$ is the direct axis reference (d-axis component of $v_{dq,ref}$), v_{ref} is the reference voltage magnitude and Q is the reactive power. The q-axis voltage reference, $v_{q,ac,ref}$ (q-axis component of $v_{dq,ref}$), is set to zero. The control block diagram using droop is shown in Fig. 3.

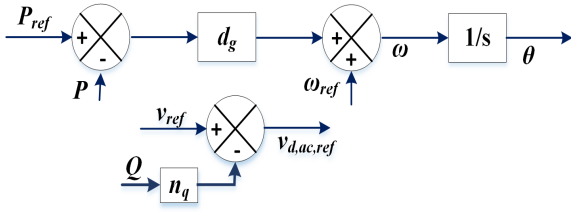


Fig. 3. Droop Control Block Diagram

The frequency (ω) and voltage (v_{ref}) references used in on-grid GFC applications are those of the grid or bus to which they are affixed [25]. The values of the parameters described so far are given in Table II [11].

TABLE II
CASE STUDY MODEL AND CONTROL PARAMETERS

Single converter module			
S_t	500 kVA	G_d, C_d	$0.83 \Omega^{-1}, 0.008 \text{ F}$
R	0.001Ω	L	$200 \mu\text{H}$
n	3	τ_{dc}	50 ms
$v_{d,ref}, v_{ll-rms}^*$	2.44, 1 kV	C	$300 \mu\text{F}$
i_{max}^d	1.2 pu(737.7A)	$i_{ac,max}$	$1.2*I_{peak}(1224.7\text{A})$
Ac current, ac voltage, and dc voltage control			
$k_{v,p}, k_{v,i}$	0.52, 3.48	$k_{i,p}, k_{i,i}$	1.48, 0.4
k_{dc}	1.6×10^3		
Droop control			
d_g	$2\pi 0.05 \text{ rad/s}$	ω_{ref}	$2\pi 50$
n_q	$1.5 * d_g$	P_{ref}	$0.3 * S_t$

III. PINN FOR GFC

A. Overview of PINN

To obtain the appropriate voltage and frequency values, the modulation index from PINN can be calculated using the $\alpha\beta$ co-ordinate image of the reference voltage signal ($v_{s,\alpha\beta,ref}$) without the need for extra controllers. Let $in \in R^{N_{in}}$ and $out \in R^{N_{out}}$ be the vectors of input and output of the PINN, which are written by

$$in = \{i_{d,m}, i_{q,m}, i_{o,m}, i_{s,d,m}, i_{s,q,m}, i_{s,o,m}, \omega, v_{d,m}, v_{q,m}, v_{o,m},$$

$$\text{error} = (v_{ref} - v), v_{gd}, v_{gq}, v_{go}, P, Q, \text{ROCOF}, \text{ROCOV}\}, \quad (14)$$

$$out = \{\hat{v}_{s,\alpha\beta,ref}\} \quad (15)$$

where $i_{d,m}$, $i_{q,m}$, and $i_{o,m}$ are the d, q, and zero axis components of GFC's current after filter, respectively, $i_{s,d,m}$, $i_{s,q,m}$, and $i_{s,o,m}$ are the d, q, and zero axis components of GFC's current before filter, respectively. $v_{d,m}$, $v_{q,m}$, and $v_{o,m}$ are the d, q, and zero axis components of GFC's voltage considering the filter's capacitor, respectively; error is the difference between the GFC's instantaneous voltage (v) and the reference voltage magnitude. v_{gd} , v_{gq} , and v_{go} are the d, q, and zero axis components of bus (to which the GFC is connected) voltage, respectively. P is the active power injected to the grid, Q is the reactive power injected to the grid, ROCOF is the rate of change of frequency of the GFC, and ROCOV is the rate of change of voltage of the GFC.

B. Key components of the PINN

1) *Data Processing:* For model training, the in and out data are loaded and transformed into Pytorch tensors.

2) *Neural Network Architecture:* Each of its three hidden layers has 128 neurons. In every hidden layer, it employs the sigmoid activation function. Except for the final layer, which stays linear, it is a forward pass, meaning that every hidden layer performs a linear transformation followed by a sigmoid activation. It consists of fully connected layers, applying transformations at each layer. For a given input x , neural network computes:

$$h^{(0)} = x \quad (16a)$$

$$h^{(l+1)} = \sigma(w^{(l)} h^{(l)} + b^{(l)}) \quad \forall l \in [0, L-1] \quad (16b)$$

$$\hat{y} = w^L h^L + b^L \quad (16c)$$

where L is the total number of hidden layers, $w^{(l)}$ and $b^{(l)}$ are the weight matrix and bias vector at layer l , $\sigma(x) = 1/(1 + e^{-x})$ is the sigmoid activation function and \hat{y} are the predicted reference voltages.

3) *Physics informed loss function:* It adds physical constraints to the standard mean squared error (MSE) loss. The model includes five components in its loss function, which are as follows:

- **Mean squared error(MSE) loss:** It is the standard loss between predicted and actual predictions

$$L_{MSE} = 1/N \sum_{i=1}^N (\hat{y}_i - y_i)^2 \quad (17)$$

where, N is the number of training samples, \hat{y}_i is the predicted output and y_i is the true reference voltage.

- **Physics informed loss:** To enforce grid-forming stability, we add voltage derivative constraints

$$L_{Physics} = E[\frac{d}{dt}v_{ref} + v] \quad (18)$$

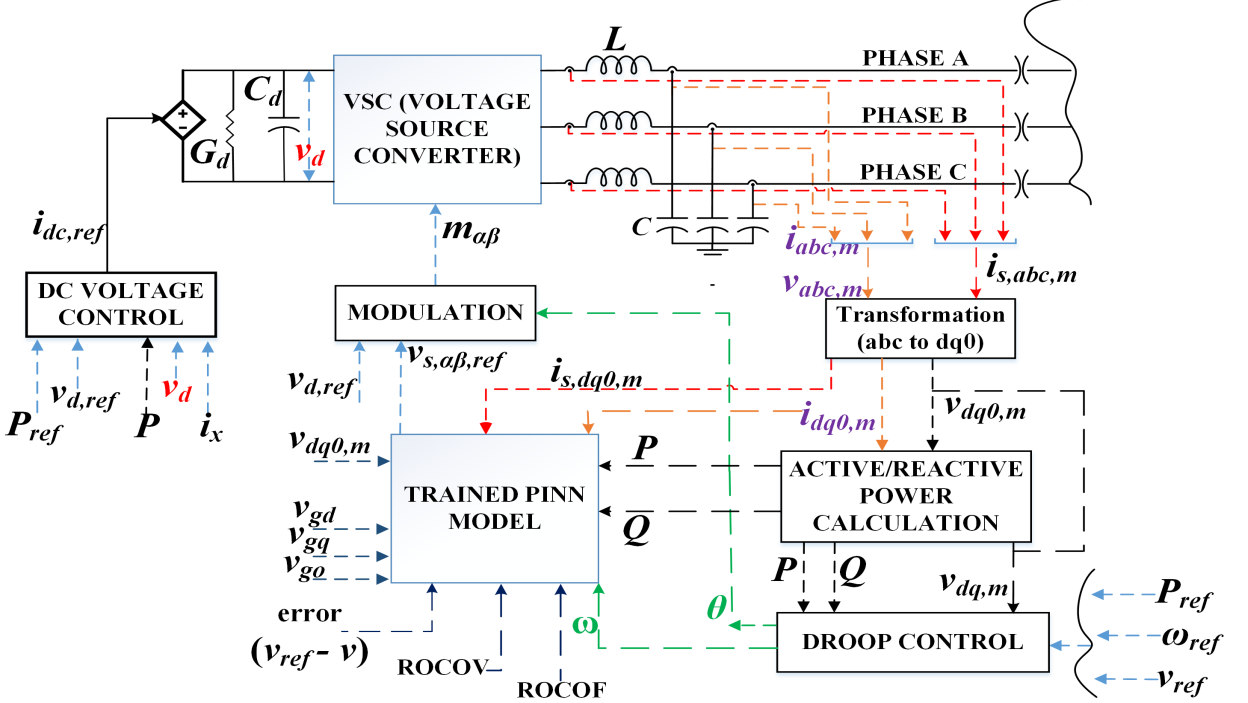


Fig. 4. Block diagram of proposed PINN-based GFC control

using automatic differentiation, we approximate $\frac{d}{dt}\hat{v}_{ref} \approx \frac{\partial\hat{v}_{ref}}{\partial t}$ which is computed using Pytorch.

- **Current limitation loss:** For inverter's safety, the model penalizes currents exceeding a certain limit, for this paper the limit is considered as the 1.2 times the peak inverter current represented by I_{peak} . The current magnitude is given by

$$I_{total} = \sqrt{I_d^2 + I_q^2 + I_o^2} \quad (19)$$

The penalty term is :

$$L_{current} = E[\max(0, I_{total} - 1.2 * I_{peak})] \quad (20)$$

where ReLU function ensures only excess currents are penalized. The ReLU (Rectified Linear Unit) function is a popular activation function in neural networks. It outputs zero for negative inputs and the input value itself for positive inputs, enabling efficient learning of complex patterns.

- **ROCOF(Rate of change of frequency) loss:** To minimize the ROCOF

$$L_{ROCOF} = 1/N \sum_{i=1}^N |X_{i,R}| \quad (21)$$

where, $X_{i,R}$ is the ROCOF input feature.

- **ROCOV(Rate of change of voltage) loss:** To minimize the ROCOV

$$L_{ROCOV} = 1/N \sum_{i=1}^N |X_{i,V}| \quad (22)$$

where, $X_{i,V}$ is the ROCOV input feature.

So, the total loss is the combination of all the loss components and given by \mathcal{L} as

$$\mathcal{L} = L_{MSE} + \lambda_{PDE} L_{Physics} + \lambda_{current} L_{current} + \lambda_{ROCOF} L_{ROCOF} + \lambda_{ROCOV} L_{ROCOV} \quad (23)$$

where λ_{PDE} , $\lambda_{current}$, λ_{ROCOF} and λ_{ROCOV} are hyperparameters controlling the weight of each term.

4) *Backpropagation and optimization:* The optimizer updates weights using the Adam optimizer, which does gradient calculation, moment estimation, Bias Correlation, and parameter update [27].

The proposed PINN-based GFC control strategy is shown in Fig. 4. The PINN model replaces the AC voltage control, AC current limitation, and AC current control while retaining the classical frequency droop mechanism.

IV. RESULTS & DISCUSSIONS

A. Simulation setup

The 13-bus microgrid that is the subject of the study is depicted in Fig. 5. It is a modified version of the standard IEEE 13-bus test feeder, with its parameters adopted from [28]. Further, the system loads are changed to match up to the requirements of the test environment.

Here, CB_i , where $i=1,\dots,5$, represents the circuit breakers and GFC_j where $j=1,\dots,4$, represents the GFCs. The circuit breaker $CB1$ is used to allow the MG to be isolated from the main grid and to operate on-grid. Circuit breakers $CB2$, $CB3$, $CB4$, and $CB5$ are used to connect and island GFCs to the 13-bus MG. As indicated in section II, the base of each GFC is set at 50 Hz and 1.5 MVA. As was mentioned, the GFCs can protect against both AC current restrictions and DC

source saturation. For each GFC, the local loads in the islanded condition are set at 0.375 MVA per GFC. The analysis of the simulation results is divided into three parts for each case study:

- **First**, CB1 is closed, while CB2, CB3, CB4, and CB5 remain open. In this configuration, the GFCs supply power solely to their local loads, and the 13-bus microgrid receives power from the grid. This part analyzes the operation of GFCs in islanded mode, supplying power to their local loads.
- **Second**, with CB1 closed, CB2, CB3, CB4, and CB5 are closed at $t = 0.8$ seconds, allowing the GFCs to operate in on-grid mode. This section analyzes the transition of GFCs from islanded to on-grid operation. The grid parameters are used for control during on-grid operation of GFCs.
- **Third**, with CB2, CB3, CB4, and CB5 closed, CB1 is opened at $t = 1.4$ seconds, causing the GFCs to supply power not only to their local loads but also to the 13-bus microgrid loads. This section examines the GFCs' capability to handle a sudden increase in power demand as they become the sole power source. During this scenario, factors such as DC source saturation and AC current limitation come into play due to the abrupt surge in power demand.

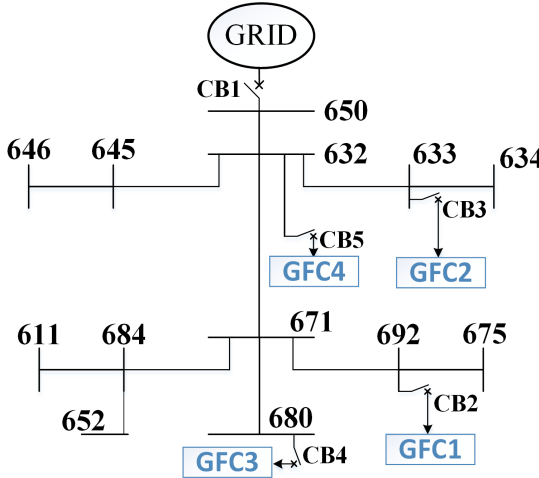


Fig. 5. Modified IEEE 13-Bus Test Feeder

MATLAB 2024b is used to implement the network in Fig. 5 in Simulink on a high-performance computer with a core i5-1245U, 1.60 GHz processor, and 16 GB of RAM. This environment is used for the PINN's training and simulation procedures as well as for the comparison strategies. The predict block in MATLAB Simulink is used to implement the trained PINN model. Where necessary, θ of (11) is used to change the coordinates for the correct input of the PINN. The PINN then uses (10) to anticipate the voltage reference, which further generates a modulation signal.

To minimize the loss function specified in (23), PINN is iteratively trained using 6000 iterations. Simulation data with variations in local GFC load and total load of 13-bus MG, along with the GFC results on droop control, as provided

by (11)(12), are used to train the model. For local loads, the variation occurs at random between 0% and 90% of the rated capacity of the GFC, and for the 13-bus MG load, it varies between 10% and 100% of the total rated capacity of all four GFCs. The data used for training the model is time series data with a fixed time step of 10 milliseconds, obtained from the system simulation shown in Fig. 5, which runs for 3 seconds.

B. Test results in modified IEEE 13-Bus Feeder

1) **Case study 1:** The performance of the traditional droop control in the system (i.e., Fig. 5) is evaluated in this case study. As illustrated in Fig. 6, the GFC maintains stability with a microgrid (MG) load of 5.916 MVA at 0.97 power factor and a local load of 0.375 MW per GFC. Under these conditions, the GFC operates effectively in both grid-connected and islanded modes. The magnitude of the output current and the controllable DC current of GFC1, as shown in Fig. 7, indicate that the GFC operates within its AC current limits.

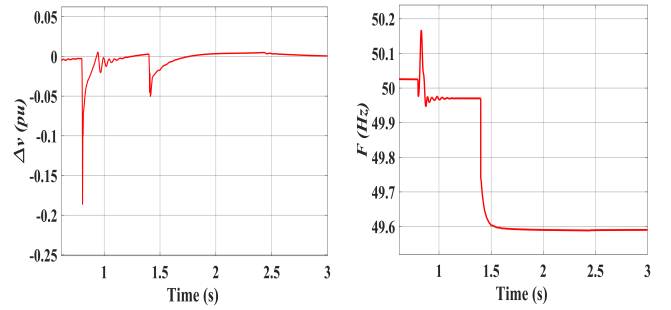


Fig. 6. Deviation of voltage and frequency of GFC1 for case study 1

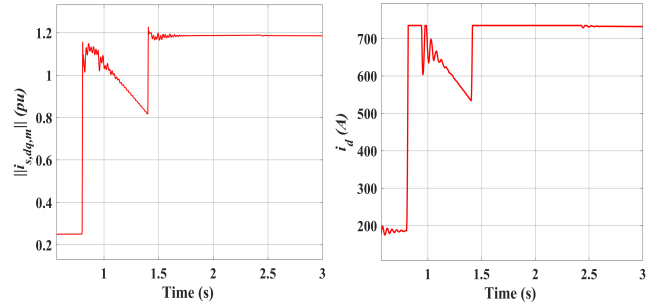


Fig. 7. Magnitude of output current and controllable DC current of GFC1 for case study 1

However, when the load is slightly increased to an MG load of 5.918 MVA at 0.97 power factor (with the local load remaining at 0.375 MW per GFC), the GFC becomes unstable in island mode after $t=1.4$ seconds, as shown in Fig. 9, due to the fixed set point of active power. The performance of the GFC begins to suffer under this load, as shown in Fig. 9. The GFC1 voltage reduces to below 5% of the steady state voltage for this load. In our study, the result of the GFC with the worst performance is displayed. Fig. 9 illustrates how the voltage drops for GFC1. Fig. 10 shows that under islanded conditions, the current flowing out of the controlled DC current source, i_d , reaches its maximum limit, $i_{d,max}^*$, at this load, even though the

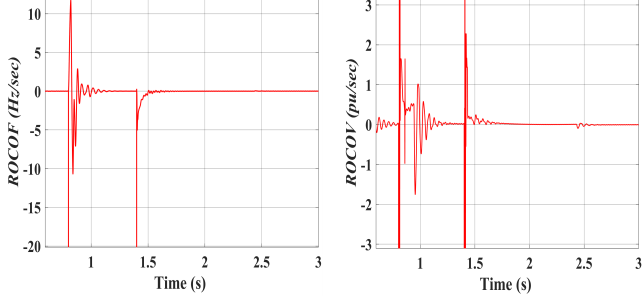


Fig. 8. ROCOF and ROCOV of GFC1 for case study 1

AC current limit, $i_{ac,max}$, is not exceeded. Fig. 11 illustrates the ROCOV and ROCOF for GFC1 in this scenario, showing a noticeable deterioration under islanded conditions compared to Fig. 8 (which shows ROCOF and ROCOV of GFC1 in stable condition).

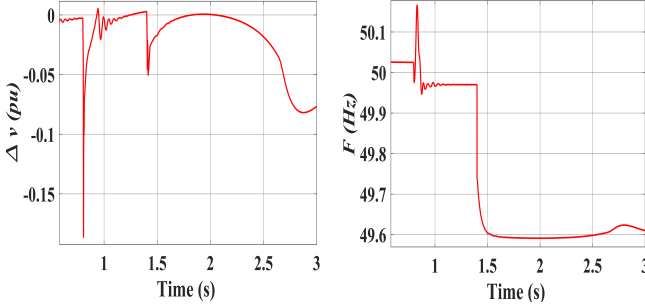


Fig. 9. Deviation of voltage and frequency of GFC1 for case study 1

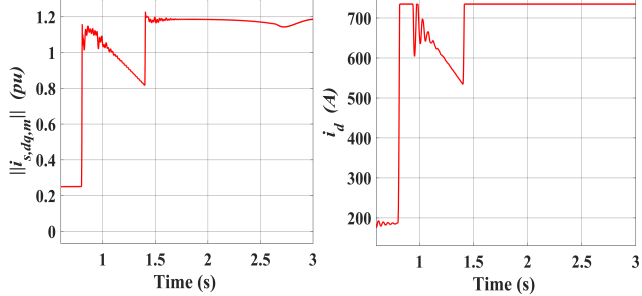


Fig. 10. Magnitude of output current and controllable DC current of GFC1 for case study 1

2) *Case study 2:* To address the stability issue observed in Case Study 1, a PINN-based control strategy is implemented in addition to frequency droop control. The loading conditions remain unchanged, where the droop control failed to stabilize the microgrid during islanding. As shown in Fig. 12, GFC1 successfully transitions from the off-grid to the on-grid mode at $t=0.8$ seconds and returns to the islanded mode at $t=1.4$ seconds. In particular, PINN-based control effectively stabilizes the system even with an MG load of 5.918 MVA at 0.97 power factor and a local load of 0.375 MW per GFC in the islanded mode. As seen in Fig. 13, in this case, i_d has not reached the maximum limit $i_{d,max}^*$ in the islanded situation. Peak voltage deviation observed during transient reduced to

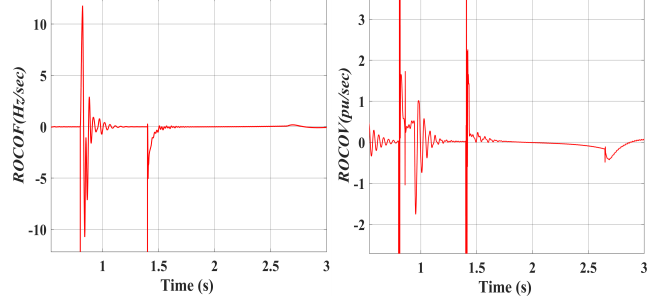


Fig. 11. ROCOF and ROCOV of GFC1 for case study 1

42.85% (i.e., from -0.05 to -0.035 as shown in Fig. 6 and Fig. 12) in this case study than in case study 1, and the MG is also successfully stabilized. The ROCOF and ROCOV for this case are also shown in Fig. 14, which is also reasonable compared to case study 1.

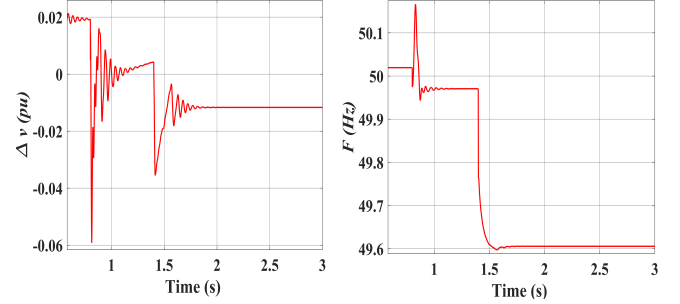


Fig. 12. Deviation of voltage and frequency of GFC1 for case study 2

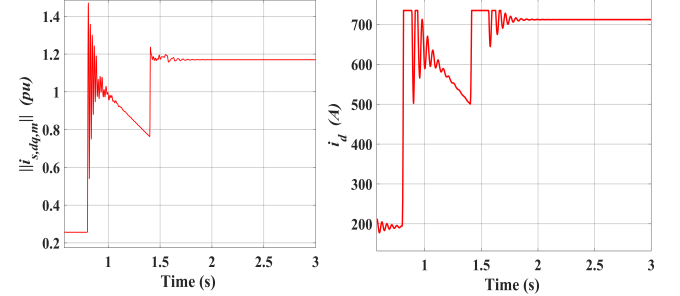


Fig. 13. Magnitude of output current and controllable DC current of GFC1 for case study 2

3) *Case study 3:* This case study compares the current limitation strategy proposed in [11] with the PINN-based control strategy introduced in this paper. Both approaches successfully stabilized the system under an MG load of 5.918 MVA at 0.97 power factor and a local load of 0.375 MW per GFC in island mode, as shown in Fig. 12 and Fig. 15. However, a key difference arises in preserving the post-disturbance operating point of the GFC, as illustrated in Fig. 16 and Fig. 17. The PINN-based control effectively stabilizes the system without altering the post-disturbance operating point as shown in Fig. 17. In contrast, the current limitation strategy proposed in [11] modifies the post-disturbance operating point since it relies on predefined threshold values to adjust the active power setpoint

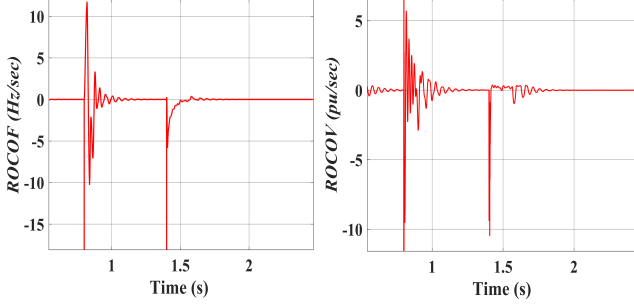


Fig. 14. ROCOF and ROCOV of GFC1 for case study 2

as shown in Fig. 16. The reliance on predefined threshold values presents a drawback: even during normal operation (at a load that consumes an AC current greater than 0.9 p.u. of the rated AC current), this strategy adjusts the active power setpoint. Consequently, this changes the system's active power and frequency, as can be seen by comparing results in Fig. 12, Fig. 15, Fig. 16, and Fig. 17. The PINN-based control improves the frequency of the system by up to 0.265 Hz (i.e., 49.605 Hz - 49.34 Hz), as shown in Fig. 12 and Fig. 15.

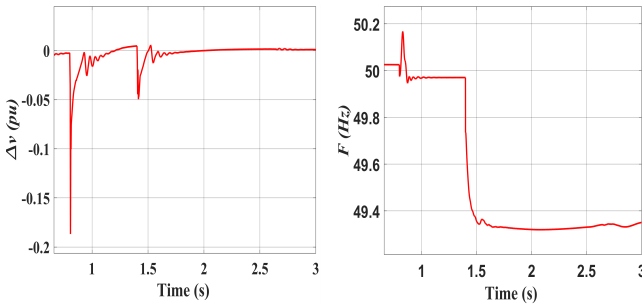


Fig. 15. Deviation of voltage and frequency of GFC1 using current limitation strategy of [11]

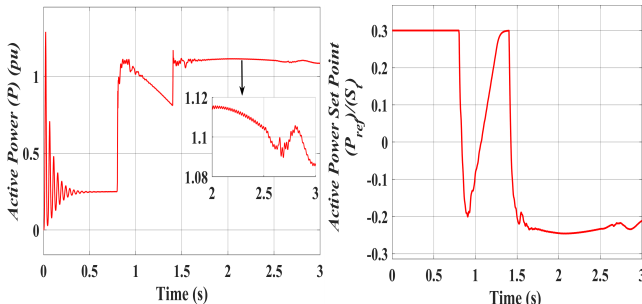


Fig. 16. Active power and Active power set point of GFC1 using current limitation strategy of [11]

4) Case study 4: This case study evaluates the effectiveness of the PINN-based control strategy for GFCs in maintaining stability under maximum sudden load changes. Through multiple simulation scenarios, it was observed that the GFCs remained stable with PINN-based control up to an MG load of 6.01 MVA at 0.97 power factor and a local load of 0.375 MW per GFC, as shown in Fig. 18. At this load level, the GFC1 reaches both its AC current limit and controlled DC

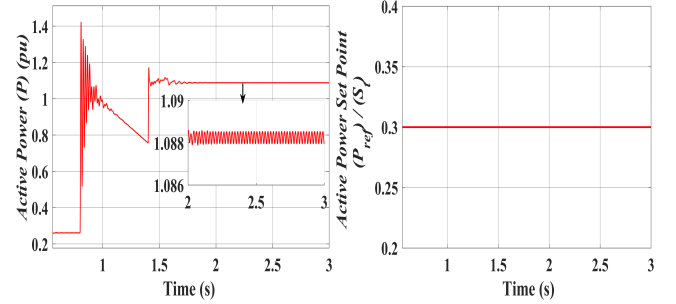


Fig. 17. Active power and Active power set point of GFC1 using PINN based control strategy

current limit, as shown in Fig. 19. Beyond this point, further load increases result in system instability, even with the PINN-based control in place. PINN can withstand a load increase of 6.01 MVA at 0.97 power factor from 5.916 MVA at 0.97 power factor compared to traditional droop control without compromising system stability, as shown in Fig. 18.

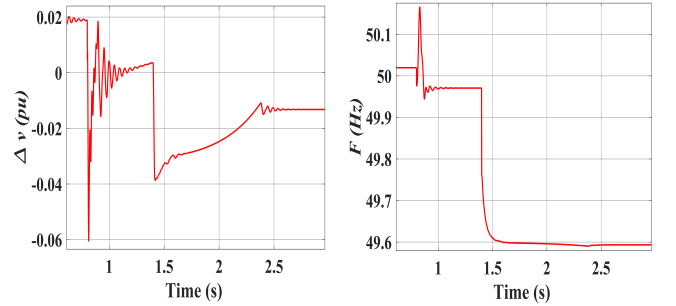


Fig. 18. Deviation of voltage and frequency of GFC1 for case study 3

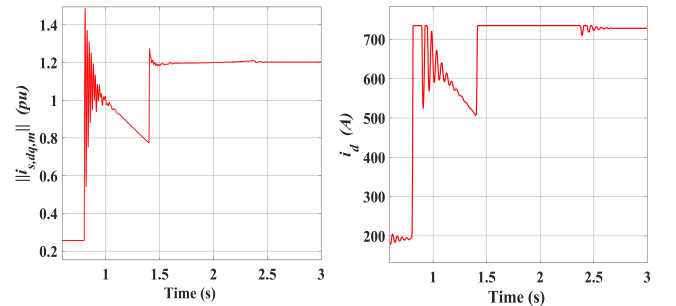


Fig. 19. Magnitude of output current and controllable DC current of GFC1 for case study 1

V. CONCLUSION

The proposed PINN provides important information to improve MG stability in situations involving DC source saturation and AC current limitation. In certain cases, integrating current limitations into the GFC may cause the droop control to become unstable due to the fixed active power set point for all loads. For robustness against overloaded conditions, PINN advancement is important. The proposed PINN efficiently preserves voltage and frequency

stability, outperforming traditional droop control. It greatly improves the stability of the MG in several situations, particularly when islanding. The PINN facilitates seamless transitions with low disturbances during grid synchronization, ensuring rapid stability and reducing transient response during resynchronization occurrences. Furthermore, during MG islanding, the suggested PINN supports both voltage and frequency.

REFERENCES

- [1] D. Pattabiraman, R. H. Lasseter, and T. M. Jahns, "Comparison of Grid Following and Grid Forming Control for a High Inverter Penetration Power System," *2018 IEEE Power & Energy Society General Meeting (PESGM)*, Portland, OR, USA, 2018, pp. 1-5.
- [2] M. C. Chandorkar, D. M. Divan and R. Adapa, "Control of parallel connected inverters in standalone AC supply systems," *IEEE Trans. Ind. App.*, vol. 29, no. 1, pp. 136-143, Jan.-Feb. 1993.
- [3] N. Pogaku, M. Prodanovic and T. C. Green, "Modeling, Analysis and Testing of Autonomous Operation of an Inverter-Based Microgrid," *IEEE Trans. Pow. Electron.*, vol. 22, no. 2, pp. 613-625, March 2007.
- [4] Q. -C. Zhong and G. Weiss, "Synchronverters: Inverters That Mimic Synchronous Generators," *IEEE Trans. Ind. Electron.*, vol. 58, no. 4, pp. 1259-1267, April 2011.
- [5] Z. Kustanovich, S. Shivratri, H. Yin, F. Reissner and G. Weiss, "Synchronverters With Fast Current Loops," *IEEE Trans. Ind. Electron.*, vol. 70, no. 11, pp. 11357-11367, Nov. 2023.
- [6] S. D'Arco and J. A. Suul, "Equivalence of Virtual Synchronous Machines and Frequency-Droops for Converter-Based MicroGrids," *IEEE Trans. Smart Grid*, vol. 5, no. 1, pp. 394-395, Jan. 2014, doi: 10.1109/TSG.2013.2288000.
- [7] S. V. Dhople, B. B. Johnson and A. O. Hamadeh, "Virtual Oscillator Control for voltage source inverters," *2013 51st Annual Allerton Conference on Communication, Control, and Computing (Allerton)*, Monticello, IL, USA, 2013, pp. 1359-1363, doi: 10.1109/Allerton.2013.6736685.
- [8] B. B. Johnson, M. Sinha, N. G. Ainsworth, F. Dörfler and S. V. Dhople, "Synthesizing Virtual Oscillators to Control Islanded Inverters," *IEEE Trans. Pow. Electron.*, vol. 31, no. 8, pp. 6002-6015, Aug. 2016, doi: 10.1109/TPEL.2015.2497217.
- [9] D. Groß, M. Colombino, J. -S. Brouillon and F. Dörfler, "The Effect of Transmission-Line Dynamics on Grid-Forming Dispatchable Virtual Oscillator Control," *IEEE Trans. Control Network Sys.*, vol. 6, no. 3, pp. 1148-1160, Sept. 2019.
- [10] C. Arghir, T. Jouini, and F. Dörfler, "Grid-forming control for power converters based on matching of synchronous machines," *Automatica*, 95, pp.273-282, 2018.
- [11] A. Tayyebi, D. Groß, A. Anta, F. Kupzog and F. Dörfler, "Frequency Stability of Synchronous Machines and Grid-Forming Power Converters," *IEEE J. Emerg. Sel. T. Pow. Electron.*, vol. 8, no. 2, pp. 1004-1018, June 2020.
- [12] K. Strunz, K. Almunem, C. Wulkow, M. Kuschke, M. Valescudero, and X. Guillaud, "Enabling 100% renewable power systems through power electronic grid-forming converter and control: System integration for security, stability, and application to Europe," *Proc. of the IEEE*, 111(7), pp.891-915, 2022.
- [13] S. Samanta, N. R. Chaudhuri, and C. M. Lagoa, "Fast frequency support from grid-forming converters under DC-and AC-side current limits". *IEEE Trans. Pow. Sys.*, 38(4), pp.3528-3542, 2022.
- [14] D. B. Rathnayake and B. Bahmani, "Multivariable Control Design for Grid-Forming Inverters With Decoupled Active and Reactive Power Loops," *IEEE Trans. Pow. Electron.*, vol. 38, no. 2, pp. 1635-1649, Feb. 2023.
- [15] A. Arjomandi-Nezhad, Y. Guo, B. C. Pal and D. Varagnolo, "A Model Predictive Approach for Enhancing Transient Stability of Grid-Forming Converters," *IEEE Trans. Pow. Sys.*, vol. 39, no. 5, pp. 6675-6688, Sept. 2024.
- [16] G. W. Chang and K. T. Nguyen, "A New Adaptive Inertia-Based Virtual Synchronous Generator with Even Inverter Output Power Sharing in Islanded Microgrid," *IEEE Trans. Ind. Electron.*, vol. 71, no. 9, pp. 10693-10703, Sept. 2024.
- [17] Mousavizade, Mirsaeed, Feifei Bai, Rasoul Garmabdi, Mohammad Sanjari, Foad Taghizadeh, Ali Mahmoudian, and Junwei Lu, "Adaptive control of V2Gs in islanded microgrids incorporating EV owner expectations." *Applied Energy* 341 (2023): 121118.
- [18] Khemmook, Panya, Krisada Prompinit, and Tossaporn Surinkaew, "Control of a microgrid using robust data-driven-based controllers of distributed electric vehicles." *Electric Power Systems Research* 213 (2022): 108681.
- [19] Abubakr, Hussein, Abderezak Lashab, Juan C. Vasquez, Tarek Hassan Mohamed, and Josep M. Guerrero, "Novel V2G regulation scheme using Dual-PSS for PV islanded microgrid." *Applied Energy* 340 (2023): 121012.
- [20] Shan, Yinghao, Jiefeng Hu, Ka Wing Chan, and Syed Islam, "A unified model predictive voltage and current control for microgrids with distributed fuzzy cooperative secondary control." *IEEE Transactions on Industrial Informatics* 17, no. 12 (2021): 8024-8034.
- [21] Baghaee, Hamid Reza, Mojtaba Mirsalim, and Gevork B. Gharehpétian, "Performance improvement of multi-DER microgrid for small-and large-signal disturbances and nonlinear loads: Novel complementary control loop and fuzzy controller in a hierarchical droop-based control scheme." *IEEE Systems Journal* 12, no. 1 (2016): 444-451.
- [22] Ngamroo, Issarachai, and Tossaporn Surinkaew, "Control of distributed converter-based resources in a zero-inertia microgrid using robust deep learning neural network." *IEEE Transactions on Smart Grid* 15, no. 1 (2023): 49-66.
- [23] Kaushal, Jitender, and Prasenjit Basak, "Power quality control based on voltage sag/swell, unbalancing, frequency, THD and power factor using artificial neural network in PV integrated AC microgrid." *Sustainable Energy, Grids and Networks* 23 (2020): 100365.
- [24] Zhang, Bin, Weihao Hu, Xiao Xu, Tao Li, Zhenyuan Zhang, and Zhe Chen, "Physical-model-free intelligent energy management for a grid-connected hybrid wind-microturbine-PV-EV energy system via deep reinforcement learning approach." *Renewable Energy* 200 (2022): 433-448.
- [25] Ngamroo, Issarachai, and Tossaporn Surinkaew, "Resiliency-Guided Grid-Forming Converter Control of Distributed Solar-Powered Electric Vehicles." *IEEE Transactions on Intelligent Transportation Systems* (2024).
- [26] Orihara, Dai, Hisao Taoka, Hiroshi Kikusato, Jun Hashimoto, Kenji Otani, Rahman Khaliqu, and Ustun Taha Selim, "Theoretical Comparison of Current Limiting Algorithms in Grid-forming Inverter in Terms of Transient Stability." *IEEE Open Journal of Power Electronics* (2024).
- [27] Huang, Bin, and Jianhui Wang, "Applications of physics-informed neural networks in power systems-a review." *IEEE Transactions on Power Systems* 38, no. 1 (2022): 572-588.
- [28] Imitiaz, Bisma, Imran Zafar, and Cui Yuanhui, "Modelling of an optimized microgrid model by integrating DG distributed generation sources to IEEE 13 Bus System." *European Journal of Electrical Engineering and Computer Science* 5, no. 2 (2021): 18-25.
- [29] Xin, Huanhai, Linbin Huang, Leiqi Zhang, Zhen Wang, and Jiabing Hu, "Synchronous instability mechanism of Pf droop-controlled voltage source converter caused by current saturation." *IEEE Transactions on Power Systems* 31, no. 6 (2016): 5206-5207.
- [30] Taul, Mads Graagaard, Xiongfei Wang, Pooya Davari, and Frede Blaabjerg, "Current limiting control with enhanced dynamics of grid-forming converters during fault conditions." *IEEE Journal of Emerging and Selected Topics in Power Electronics* 8, no. 2 (2019): 1062-1073.